JACS Au
AN OPEN ACCESS JOURNAL OF THE AMERICAN CHEMICAL SOCIETY

pubs.acs.org/jacsau

Article

Alumina Graphene Catalytic Condenser for Programmable Solid Acids

Tzia Ming Onn, Sallye R. Gathmann, Yuxin Wang, Roshan Patel, Silu Guo, Han Chen, Jimmy K. Soeherman, Phillip Christopher, Geoffrey Rojas, K. Andre Mkhoyan, Matthew Neurock, Omar A. Abdelrahman, C. Daniel Frisbie, and Paul J. Dauenhauer*

Cite This: *JACS Au* 2022, 2, 1123–1133

Read Online

ACCESS | Metrics & More | Article Recommendations | Supporting Information

ABSTRACT: Precise control of electron density at catalyst active sites enables regulation of surface chemistry for the optimal rate and selectivity to products. Here, an ultrathin catalytic film of amorphous alumina (4 nm) was integrated into a catalytic condenser device that enabled tunable electron depletion from the alumina active layer and correspondingly stronger Lewis acidity. The catalytic condenser had the following structure: amorphous alumina/graphene/HfO_2 dielectric (70 nm)/p-type Si. Application of positive voltages up to +3 V between graphene and the p-type Si resulted in electrons flowing out of the alumina; positive charge accumulated in the catalyst. Temperature-programmed surface reaction of thermocatalytic isopropanol (IPA) dehydration to propene on the charged alumina surface revealed a shift in the propene formation peak temperature of up to ΔT_{peak}~50 °C relative to the uncharged film, consistent with a 16 kJ mol^{-1} (0.17 eV) reduction in the apparent activation energy. Electrical characterization of the thin amorphous alumina film by ultraviolet photoelectron spectroscopy and scanning tunneling microscopy indicates that the film is a defective semiconductor with an appreciable density of in-gap electronic states. Density functional theory calculations of IPA binding on the pentacoordinate aluminum active sites indicate significant binding energy changes (ΔBE) up to 60 kJ mol^{-1} (0.62 eV) for 0.125 e^- depletion per active site, supporting the experimental findings. Overall, the results indicate that continuous and fast electronic control of thermocatalysis can be achieved with the catalytic condenser device.

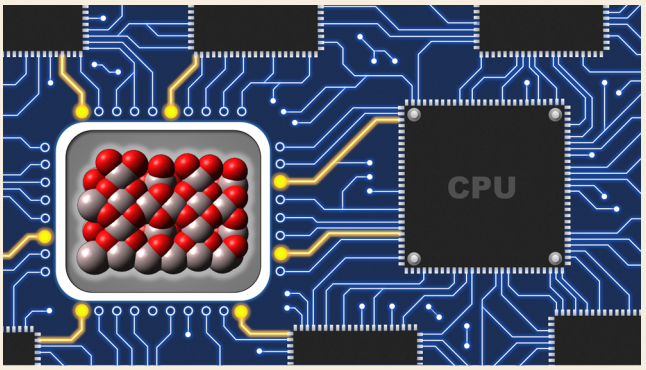

KEYWORDS: *catalysis, dehydration, alumina, catalytic condenser, graphene*

INTRODUCTION

Manipulation of charge within catalytic materials permits tunable surface chemistry and electronic optimization of chemical reaction rates.[1] Here, we put forward the concept of "catalytic condensers" that allow for reversible tuning of charge density in a catalyst thin film by means of an applied voltage. The catalyst film, in this case, an amorphous 4 nm thick layer of alumina, is deposited on top of a graphene/insulator/conductor stack, and application of a voltage between graphene and the bottom electrode induces charge in the catalyst, thereby tuning the surface catalytic chemistry. The extent of hole/electron density accumulated in the catalyst layer depends on the applied potential, composition, and electronic characteristics of the dielectric and catalyst films, as well as quality of film deposition. We propose that this will be a generally applicable strategy for manipulating the reactivity of catalyst thin films that can be tuned for different heterogeneous chemistries under static or dynamic modulation.

Precedents for this work include the traditional metal-oxide-semiconductor field effect transistor that alters charge carrier density in semiconductor layers with high-*k* dielectric oxide layers; gate potential variation manipulates the electronic bands and the charge density of the semiconductor to achieve high and low conductivity.[2] This device structure has been used recently to manipulate the conduction band edge position and electron accumulation in ultrathin ZnO layers in electrochemical devices. In that case, a 5 nm ZnO film on a 300 nm SiO_2 dielectric layer allowed for electron accumulation throughout the entire ZnO layer, such that the exposed top surface of ZnO, which was in contact with the electrolyte, exhibited tunable rates of electron transfer with a soluble redox agent, tetrabromo-1,4-benzoquinone.[3] This transistor method-

Received: February 20, 2022
Revised: March 27, 2022
Accepted: April 1, 2022
Published: May 7, 2022

https://doi.org/10.1021/jacsau.2c00114
JACS Au 2022, 2, 1123–1133

ology was also applied to two-dimensional (2D) semiconductor crystals such as single layer (SL) MoS_2 incorporated in a MoS_2/SiO_2/p-Si stack, wherein charge modulation of active sites (S vacancies) was shown to increase the activity of electrocatalytic hydrogen evolution by a factor of 4.[4−6] However, to our knowledge, the use of capacitive charging to enhance thermocatalytic activity has not been reported.

Here, we consider a catalytic condenser comprised of an ultrathin film of alumina, a metal oxide catalyst commonly used to carry out acid-catalyzed chemical transformations, such as alcohol dehydration[7−9] and as a support for metal catalysts.[10,11] As depicted in Scheme 1, the amorphous alumina film (4 nm) supported on graphene is separated from a conductive p-type silicon wafer by 70 nm of HfO_2 dielectric. When a voltage V_{CAT} is applied, charge accumulated in the bottom silicon electrode is balanced by a countercharge in the thin catalytic alumina/graphene film (as in a typical capacitor or condenser). Because of the extreme thinness of the alumina layer, its accumulated charge is accessible to reactive fluids (adsorbates in plasmas, vapors, gases, and liquids) on the top surface. The tunable activity of the alumina catalyst derives from the accumulated charge, which is controlled by V_{CAT}.

Scheme 1. Charge Condensation in the Catalyst Alumina/Graphene Active Surface Layer of a Thin Film Catalytic Condenser

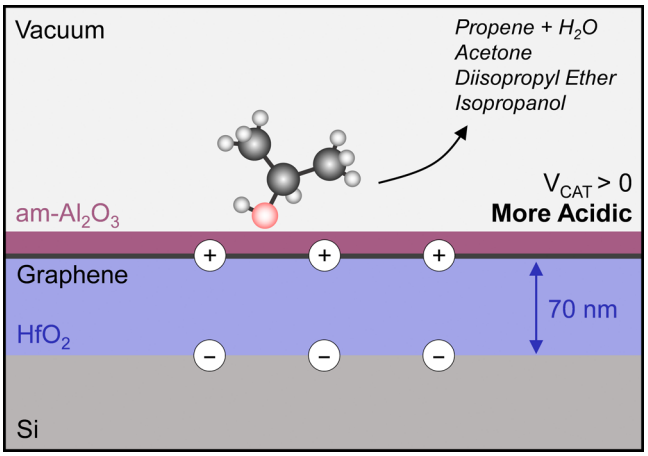

Alumina as the active layer within the catalytic condenser is desirable because it is a commonly used solid Lewis acid catalyst.[12,13] However, *bulk* alumina is an electronic insulator with a band gap of 8.7 eV,[14−16] with valence and conduction bands far from the Fermi level. Thus, it is not obvious that charge can be accumulated in an alumina film in a condenser stack. However, the insulating nature of alumina is a function of its structure. For example, the (100) and (110) surfaces of crystalline γ-Al_2O_3 are predicted to have valence bands near the Fermi level and band gaps of only ∼3 eV.[17] Similarly, the band gap for ultrathin (7−10 nm) films of *amorphous* alumina has been measured to be 2.5 eV, which is in the semiconductor range.[15] We will demonstrate below that the alumina we deposit can be viewed as a defective semiconductor, and so, charge accumulation is possible.

In this work, the device shown in Scheme 1 was developed and evaluated experimentally and theoretically to understand the degree of electronic control that could be achieved for a model catalytic reaction, isopropanol (IPA) dehydration. On alumina surfaces, IPA is thought to adsorb and react on pentacoordinate Lewis acid sites (Al_V^{3+}) with activity that correlates with acid strength, dictated by the partial positive charge (δ^+) on the surface aluminum and partial negative charge on the bonded oxygen (δ^-).[18] IPA dehydrates on alumina predominately unimolecularly to propene and water with minimal formation of either acetone via dehydrogenation or diisopropyl ether via bimolecular dehydration. Here, electronic modulation of the active site chemistry was interrogated by experimental and theoretical calculations, evaluating the charge accumulated in the catalytic layer and its effect on IPA dehydration kinetics as a function of device design and applied potential bias. Application of potential bias of +3 V is shown here to dramatically enhance the surface acidity of the catalytic layer and lower the reaction temperature. These results are presented following a thorough description of the device design and characterization.

RESULTS AND DISCUSSION

The alumina−graphene catalytic condenser device depicted in Scheme 1 and Figure 1a was fabricated with full synthetic details available in the methods section and the Supporting Information (Figures S1 and S2). On top of the p-type Si substrate, a ∼70 nm HfO_2 dielectric layer was grown by atomic layer deposition (ALD) at 100 °C using a flow-type ALD reactor. The growth rate of the HfO_2 film, as measured by spectroscopic ellipsometry (Figure S3), was consistent with literature values.[19,20] Next, graphene was transferred onto the HfO_2 layer using a previously reported polymethyl methacrylate (PMMA)-based method,[21,22] leaving a ca. 1.0 cm^2 conductive sheet across the device. To make good electrical contact to graphene, a small area (0.01 cm^2) contact (Au/Ti, 45 nm/5 nm) was deposited on the graphene by e-beam evaporation through a shadow mask. Finally, the ∼4 nm catalytic alumina layer was grown via ALD at 100 °C using the same flow-type ALD reactor as mentioned above.

Cross-sectional transmission electron microscopy (TEM) and high-angle annular dark-field (HAADF) scanning TEM (STEM) images, combined with compositional analysis using energy-dispersive X-ray (EDX) spectroscopy, confirmed the layered structure of the catalytic condenser device, as shown in Figures 1b−d and S4. From the cross section, as expected, a multilayer (ML) of graphene was observed between the HfO_2 and the alumina layer, which was 0.4 nm thick. The aluminum oxide layer appears to be predominantly amorphous, as anticipated for films made by ALD at low deposition temperatures.[19,23,24] There were some regions, as identified in Figure S5, where surface HfO_2 formed crystalline grains ∼10 nm in diameter at the interface, possibly during the device fabrication process. Scanning electron microscopy (SEM) analysis in Figures 1c and Figure S6 confirms that the alumina film above the graphene is continuous across the device. The successful growth of the aluminum oxide layer on the graphene could be attributed to the use of H_2O in ALD, which created OH sites on the graphene surface at low deposition temperatures.[25−27] The presence of a continuous alumina layer over large lateral dimensions (∼0.1 μm) with thicknesses of ∼4 nm was further confirmed by atomic force microscopy (AFM). It should be noted that at large lateral scales of order 1 cm, graphene is expected to have wrinkles and folds, which were observed in our SEM−EDX analysis (Figures 1c and S6), resulting from its chemical vapor deposition (CVD) growth on the initial Cu substrate[28] and its transfer. Hexagonal domains,

https://doi.org/10.1021/jacsau.2c00114
JACS Au 2022, 2, 1123−1133

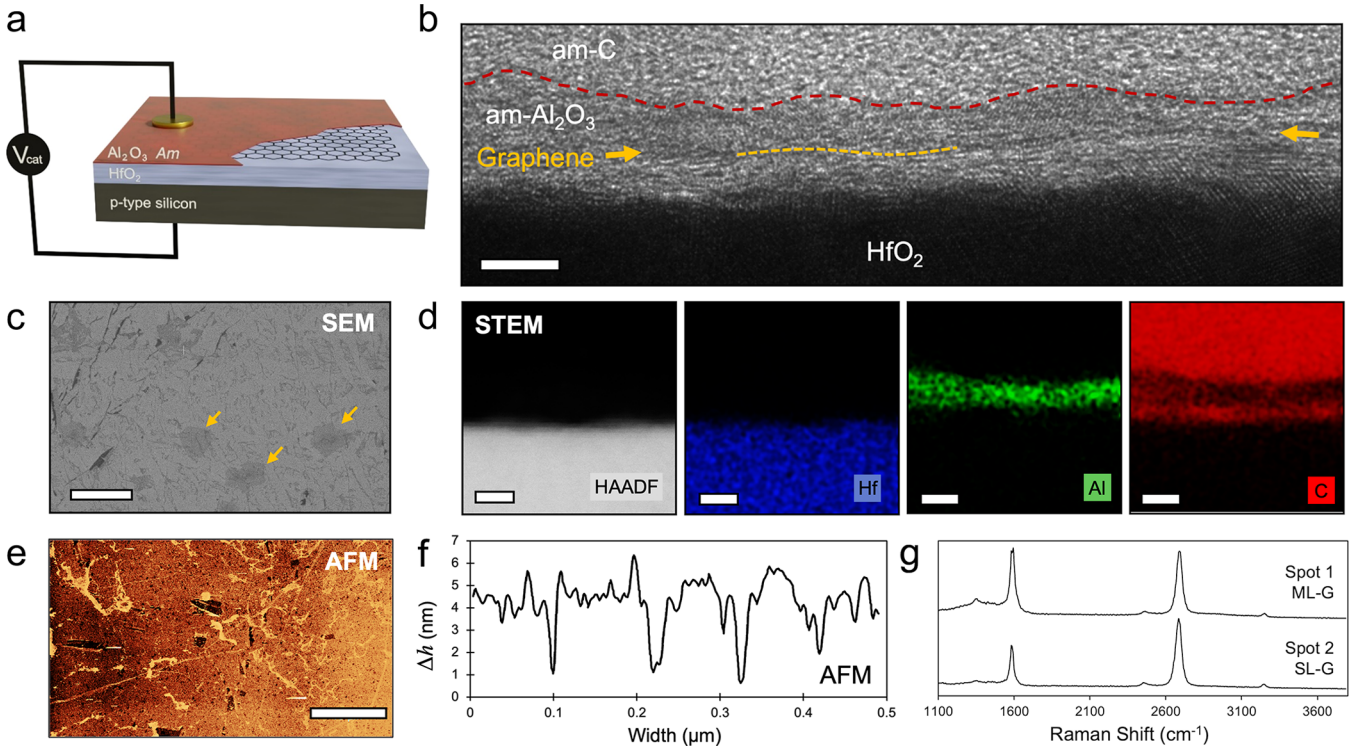

Figure 1. Alumina catalytic condenser design and composition. (a) Schematic illustration of the device showing a 70 nm thick HfO_2 layer sandwiched between the p-type silicon substrate and a thin (4 nm) graphene/alumina bilayer. (b) Conventional bright-field TEM image of the device cross section showing all the functional layers in the stack: HfO_2, graphene, and am-Al_2O_3. The scale bar is 5 nm. The red dashed line shows the boundary between the am-Al_2O_3 and deposited protective am-C layer. The yellow arrows and dashed line highlight the location of the graphene layer. (c) Top-view SEM image of the device. The cracks in the graphene are visible as dark contrast. Yellow arrows show the hexagon-shaped second layers of graphene. The scale bar is 25 μm. (d) HAADF-STEM image and the complementary EDX elemental maps from layer stack: Hf (blue), Al (green), and C (red). The C signal from graphene can be seen under the am-Al_2O_3 layer. The C signal above am-Al_2O_3 is from the deposited am-C protection layer. The scale bar is 5 nm. (e) AFM image and (f) height profile of the condenser device. The scale bar is 1 μm. (g) Raman spectra of graphene collected at different sites on the device. Spot 1 is a representative spectrum of ML graphene, whereas Spot 2 is a representative spectrum of SL graphene.

also visible on these SEM images (Figures 1c and S6), represent additional graphene layers, indicating that these transferred graphenes are composed of regions of monolayers and bilayers/trilayers. Raman spectra measured over 30 spot sites on the device (Figure 1g) validated the existence of monolayer graphene and bilayers/trilayers based on the intensity ratio of the G (1587 cm^{-1}) and 2D (2658 cm^{-1}) band and showed minimal defects due to the weak D band intensity (1350 cm^{-1}). Spot 1 is a representation of bilayer graphene with the ratio of intensity I_{2D}/I_G of ~1, whereas spot 2 represents a monolayer of graphene with the I_{2D}/I_G of ~2.

A high quality HfO_2 dielectric layer is important for voltage-tunable thermocatalysis to ensure that charges are distributed uniformly along the graphene−catalyst layer. A particular consideration is a possible change in the HfO_2 film structure during programmed temperature ramps, which were used in our reaction analysis described later. Consequently, the thermal stability of the HfO_2 film in the catalytic capacitor device was assessed by measuring the X-ray diffraction (XRD) pattern of the HfO_2-Si structure as a function of temperature, as shown in Figure 2a. These HfO_2-Si samples were heated in a muffle furnace under ambient conditions for 1 h at different temperatures prior to XRD data collection. The 70 nm HfO_2 XRD-amorphous ALD films were heated from 100 to 350 °C; the films started to crystallize *only* after heating above 400 °C. The detected peaks were associated with the monoclinic polymorphs of HfO_2, with the crystallites aligning preferentially along certain Miller indices. This is expected because selection of substrate composition, substrate orientation, deposition temperature, and choice of precursors are known to affect the crystallization process and structural orientation of ALD films.[29] Crystallite formation above 400 °C is known to impact the HfO_2 structural integrity, increase surface roughness, introduce pinholes, and affect the electronic properties.[30−34] So, practically speaking, 400 °C is an upper bound for examining catalytic behavior in these particular devices.

To further establish a working temperature range for the catalytic condenser, the dielectric constant and capacitance of HfO_2 were determined as a function of processing temperature (Figure 2b). For the electrical measurements, a metal-HfO_2-Si capacitor was fabricated by depositing a 0.01 cm^2 Au/Ti metal contact (45 nm/5 nm) via shadow-masked e-beam evaporation on HfO_2-Si after the samples were heat-treated at selected temperatures. At low treatment temperatures (100−300 °C), a specific capacitance of ~330 nF cm^{-2} was calculated from experimental displacement current−voltage curves (Figures 2b, S8 and S9) at varying sweep rates (0.25−1.25 V/s); this specific capacitance decreased to ~200 nF cm^{-2} for treatment at 400 °C. This corresponds to dielectric constants of ~26 and ~16 (Figure 2b) as the HfO_2 layer converted from amorphous to crystalline states, in agreement with the range of reported dielectric constants of bulk HfO_2.[23,24,35] It must be noted that

https://doi.org/10.1021/jacsau.2c00114
JACS Au 2022, 2, 1123−1133

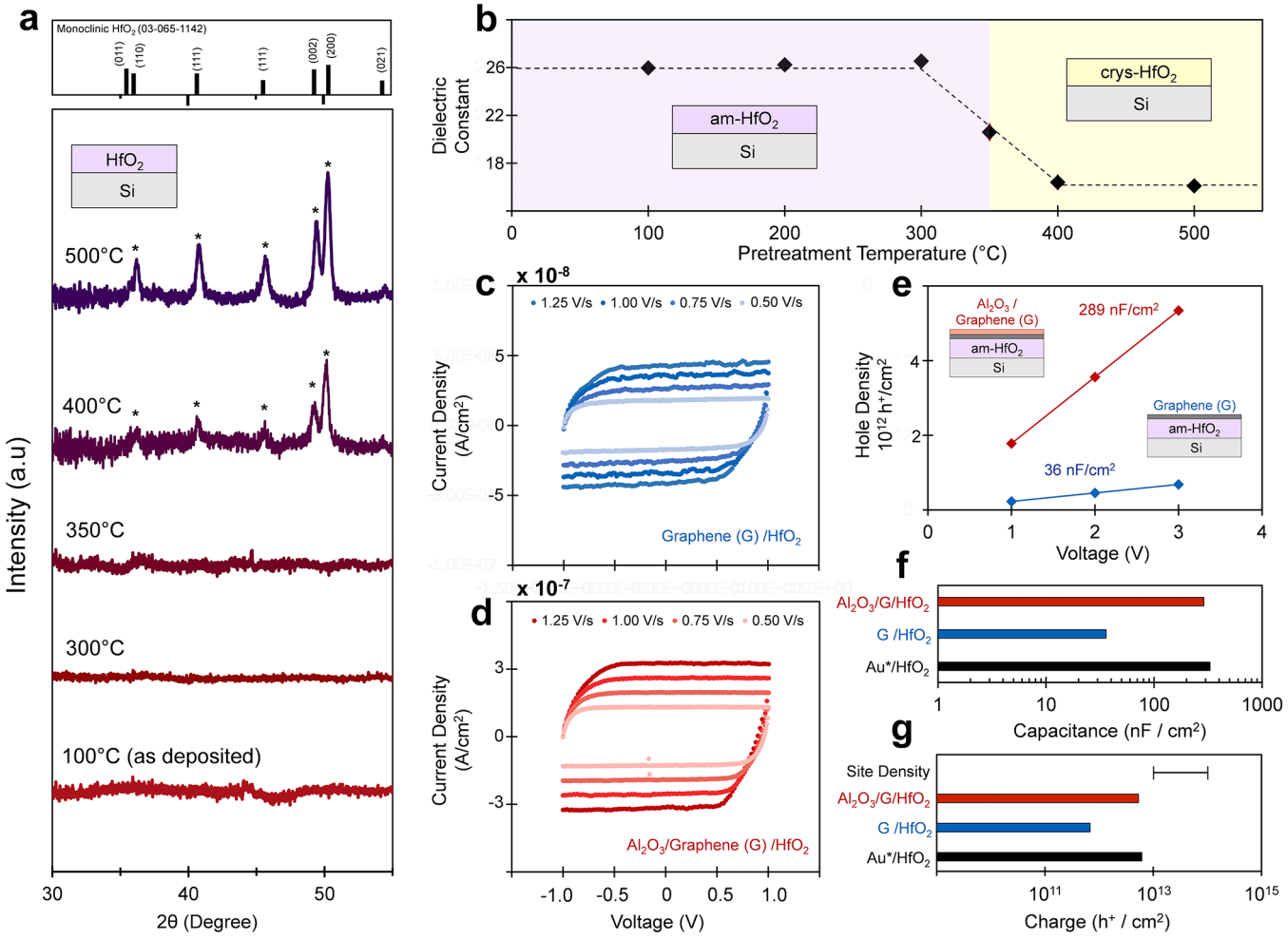

Figure 2. Characterization of the alumina−graphene catalytic condenser device. (a) XRD patterns of ALD-HfO_2 on Si after being heated in air. Peaks associated with crystallized monoclinic HfO_2 are shown as the reference. (b) Average dielectric constant of HfO_2 as a function of annealing pretreatment temperature in air. The capacitive current density for each point can be found in Figure S8. A change in capacitive current density occurs at ∼350 °C before the ALD HfO_2 film begins to crystallize. (c) Capacitive displacement current density of graphene/HfO_2/Si as a function of voltage bias at different voltage sweep rates. (d) Capacitive current density of alumina/graphene/HfO_2/Si as a function of voltage and sweep rates. (e) Average number of induced holes on graphene (blue) and alumina−graphene (red) as a function of V_{CAT}. Error bars are within the size of the data point. (f) Averaged capacitance of the catalytic condenser with varying active layers above HfO_2: Au* (Au/Ti contact, 45 nm/5 nm), graphene (blue), and alumina on graphene (Al_2O_3/G, red). (g) Number of holes on the catalytic condenser at +3 V with varying active layers above the HfO_2 layer; the estimated catalytic active site density of alumina is provided for comparison (purple, sites/cm^2). Au*/HfO_2 denotes an Au/Ti contact (45/5 nm) on HfO_2.

there was significant current leakage *only* after heating above 400 °C, again confirming that 400 °C is an upper limit for reaction studies.

To assess charge accumulation in our catalytic condensers, we performed additional displacement current measurements on two different condenser stacks, one without aluminum oxide (graphene/HfO_2/p-Si) and the other being the complete catalytic condenser (alumina/graphene/HfO_2/p-Si). Displacement currents as a function of voltage and sweep rate for both stacks are shown in Figure 2c,d, respectively, and analysis of these curves leads to the electron density versus voltage plot shown in Figure 2e. As expected, the stored electron density in the devices increases linearly with voltage, V_{CAT}. Note that for the alumina/graphene device shown in red that the maximum electron density is nearly 5.3 × 10^{12} e$^-$/cm^2. Note also that the slope observed in Figure 2e is the specific capacitance. It is evident that the device with the alumina/graphene top contact has an eightfold larger capacitance than the device with just graphene as the top contact layer (289 vs 36 nF cm^{-2}). In other words, the charge accumulated in the condenser is substantially larger when alumina is present, which is not unexpected as the electronic density of states in the ultrathin graphene is likely insufficient to fully screen the applied electric field.[36] The alumina layer provides additional density of states and thus larger charge accumulation.

A direct comparison of capacitances and maximum charge density at V_{CAT} of +3 V for the three types of stack devices discussed above is shown in Figure 2f,g. It is noteworthy that the condensers with Au versus alumina/graphene top contacts are comparable in capacitance and charge accumulation. Because the capacitances of the graphene-only versus the alumina/graphene devices are so different, we infer that the majority of the induced charge in the alumina/graphene device is actually in the alumina and therefore available to impact surface thermochemistry.

https://doi.org/10.1021/jacsau.2c00114
JACS Au 2022, 2, 1123−1133

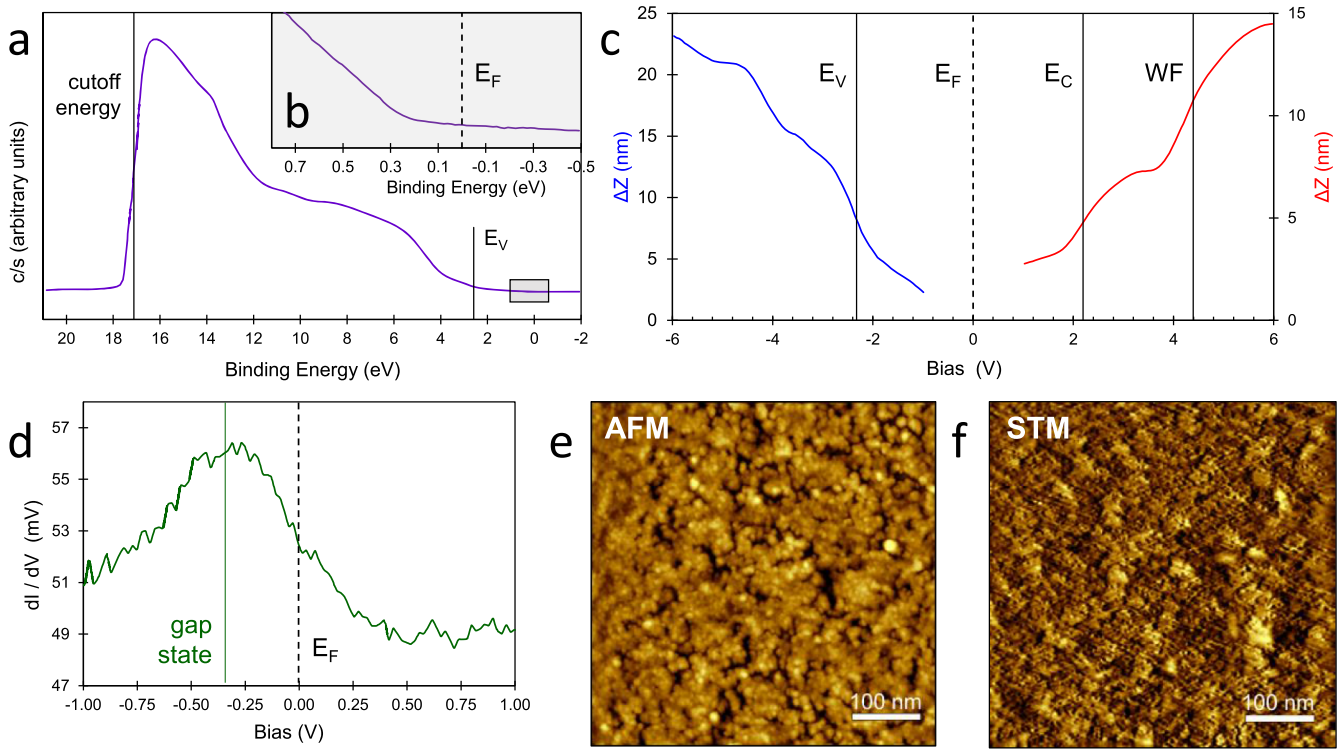

Figure 3. Electronic Characterization of the Alumina/Graphene Layer by UPS and STM. (a) UPS with energy cutoff for work function and valence band onset (2.3 eV) highlighted. (b) Magnified view of the UPS data near the Fermi level shown in the inset. The slope change near 0.25 eV indicates the presence of in-gap states above the valence band edge. (c) STM constant-current distance−voltage curves for the alumina/graphene film with valence band edge (E_V = −2.3 eV), conduction band edge (E_C = 2.2 eV), and work function (WF = 4.4 eV) identified. (d) Differential conductance near E_F revealing a discrete gap state (~300 meV). (e) AFM and (f) STM image (tip bias = −710 mV, I = 622 pA) of the alumina surface showing similar morphologies.

Alumina Film Electronic Characteristics

The electronic states of the top layer of the alumina−graphene catalytic condenser were characterized by ultraviolet photoelectron spectroscopy (UPS) and scanning tunneling microscopy (STM), as depicted in Figure 3. Based on the UPS spectra, the ALD-deposited alumina thin film is electronically very different from insulating bulk Al_2O_3. The UPS spectrum in Figure 3a indicates the valence band edge (E_V) is at 2.3 eV below the Fermi level. However, closer inspection between −0.5 and +0.8 eV in Figure 3b indicates the presence of in-gap states near the Fermi level at ~250−350 meV. These gap states are present on the surface of the alumina even for devices without graphene, as shown in Figure S7.

The electronic states of the alumina−graphene catalytic condenser active layer were further probed by STM in Figure 3c−f. While bulk crystalline alumina is an insulator, the ~4 nm alumina film in the condenser was sufficiently conductive for mapping via STM (Figure 3f); the resulting image was consistent with the morphology of the surface observed by AFM with the same resolution (Figure 3e). The electronic characteristics of the surface at large biases were evaluated as constant-current distance−voltage curves (Figure 3c), identifying the valence band edge (E_V of −2.3 eV), the conduction band edge (E_C of 2.2 eV), and the work function (WF of 4.4 eV). It is clear from Figure 3c that the amorphous alumina film has a band gap of ~5 eV, much smaller than crystalline γ-Al_2O_3, which has a band gap over 8 eV.[14−16] Furthermore, STM differential conductance measurements under varying bias (Figure 3d) also indicated a gap state about 300 meV below the Fermi level, in general accordance with the UPS spectrum of Figure 3b.

The combined spectroscopy data of Figure 3 point to the existence of in-gap electronic states in the alumina film that can be occupied by (or depleted of) electrons. These in-gap electronic states exist with sufficient density to permit STM imaging via tunneling current between the STM tip and the aluminum oxide film. The ALD-deposited alumina film acts much like a "poor insulator" or defective semiconductor, allowing charge to pass through the layer to the conductive graphene layer below. Graphene can move charge laterally across the surface of the device, and the aluminum oxide in turn has sufficient defect state densities near the Fermi level to conduct in the normal direction.

Catalytic Condenser Alumina Surface Chemistry

The unique chemical properties of the catalytic condenser's alumina film were then characterized by thermocatalytic dehydration of IPA. Catalytic properties of the alumina−graphene condenser were probed through temperature-programmed surface reaction (TPSR) under varying voltage bias; details of the TPSR experimental design and method are provided in the Supporting Information (Figures S11−S17). Briefly, the catalytic condenser was housed within a chamber capable of evacuation to ultrahigh vacuum (UHV, ~10^{-9} Torr, Figure S13), where IPA was dosed into the chamber to adsorb on the alumina film; 24 h of pumping removed physisorbed IPA from the chamber, leaving chemisorbed IPA on the aluminum oxide active sites. As the alumina/graphene condenser surface temperature was increased, aluminum

https://doi.org/10.1021/jacsau.2c00114
JACS Au 2022, 2, 1123−1133

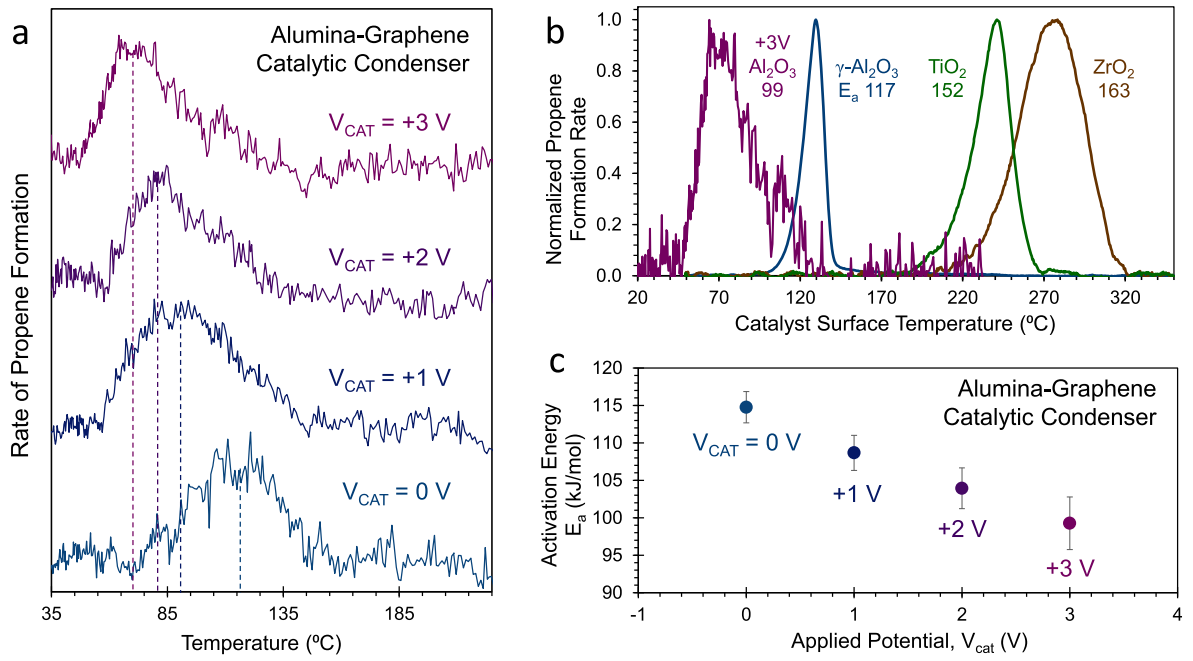

Figure 4. TPSR of IPA dehydration. (a) Temperature-programmed IPA dehydration on the alumina catalytic condenser device (4 nm alumina/graphene/70 nm HfO_2/p-type Si) to form propene at varying applied voltages, V_{CAT}. (b) Temperature-programmed IPA dehydration to propene on the catalytic condenser at V_{CAT} of +3 V and the powders of γ-alumina, titania, and zirconia with activation energy, E_a (kJ mol^{-1}), to form propene determined by the Redhead equation. (c) Activation energy, E_a, of propene formation from IPA on the alumina catalytic condenser as determined by the Redhead equation. Error bars represent a 90% confidence interval.

oxide catalyzed the dehydration of chemisorbed IPA, which was followed by mass spectrometry. The propene signal was tracked at a mass-to-charge (m/z) ratio of 41, correcting for the influence of simultaneously desorbing unreacted IPA (m/z = 45, Figure S19) and subtraction of a sigmoidal baseline derived from the chamber pressure; full details are provided in the Supporting Information. Catalyst surface temperature was measured using a type-K thermocouple placed near the location of the catalytic condenser within the UHV chamber (Figures S16 and S17).

Under UHV-TPSR conditions, unimolecular IPA dehydration to propene over the alumina catalytic condenser is the dominant pathway, with negligible formation of acetone and diisopropyl ether through dehydrogenation and bimolecular dehydration, respectively. The dominance of unimolecular dehydration was consistent with ambient pressure TPSR over bulk alumina powders, where 99% selectivity to propene as the product of unimolecular dehydration was observed (Table S1). Additionally, IPA dehydration kinetics on the 1 cm^2 alumina catalytic condenser, in the absence of applied potential bias, was found to be in agreement with γ-alumina powder catalysts. Without applied potential bias, the rate of propene formation on the alumina condenser peaked at ∼130 °C (T_{peak}, Figures 4a and S18). Applying a first-order Polanyi−Wigner equation to the zero-bias experimental TPSR profile,[37] an activation energy (E_a) of 115 ± 1 kJ mol^{-1} (1.19 eV) for IPA unimolecular dehydration over the alumina condenser was measured in the absence of a potential bias (V_{CAT} = 0 V, Figure 4c). Similarly, we measured an activation energy of 117 ± 1 kJ mol^{-1} (1.21 eV) for unimolecular IPA dehydration over bulk γ-alumina powder via ambient pressure TPSR (Figure 4b), consistent with prior measurements by Gorte and co-workers.[13]

Condensation of holes (positive charge) for catalytic modulation of alumina was then evaluated by IPA dehydration TPSR under V_{CAT} biases of 0, +1, +2, and +3 V. Our central result is that application of positive voltage bias (V_{CAT} > 0 V) significantly reduced the peak temperature of the rate of propene formation (Figure 4a). While propene formation peaked at ∼130 °C under zero bias (V_{CAT} of 0 V), propene formation peak temperatures reduced by as much ∼50 °C (ΔT_{peak}) at V_{CAT} of +3 V; the process was reversible when the voltage was reverted to V_{CAT} of 0 V. The change in peak temperature is commensurate with a change in the kinetics of IPA unimolecular dehydration; positive potential bias reduced the activation energy to 109 ± 2, 104 ± 3, and 99 ± 4 kJ mol^{-1} for V_{CAT} of +1, +2, and +3 V, respectively, constituting an overall reduction in the activation energy (ΔE_a) from V_{CAT} of 0 V of ∼16 kJ mol^{-1} (0.16 eV, Figure 4c). It is worth noting that in the absence of an aluminum oxide layer, no propene formation was observed in the course of a TPSR (Figures S20 and S21).

One potential explanation for the experimentally observed higher activity for unimolecular IPA dehydration over the graphene-alumina catalytic condenser is ohmic heating of the active surface. Charge separation across the 70 nm HfO_2 insulating layer introduces the possibility for "leakage current" through the dielectric, potentially leading to resistive heating of the catalytic layer. We have demonstrated earlier that leakage current is negligible when HfO_2 is maintained below 400 °C. The power supply (Keithley 2450) applying the potential bias to the active device surface during the experiment was limited to 105 μA to eliminate thermal artifacts due to ohmic heating. The possibility of ohmic heating of the catalytic condenser was also experimentally evaluated by measuring the surface temperature of the catalytic condenser with an infrared camera (FLIR A655) under varying potential bias (Figure S22);

https://doi.org/10.1021/jacsau.2c00114
JACS Au 2022, 2, 1123−1133

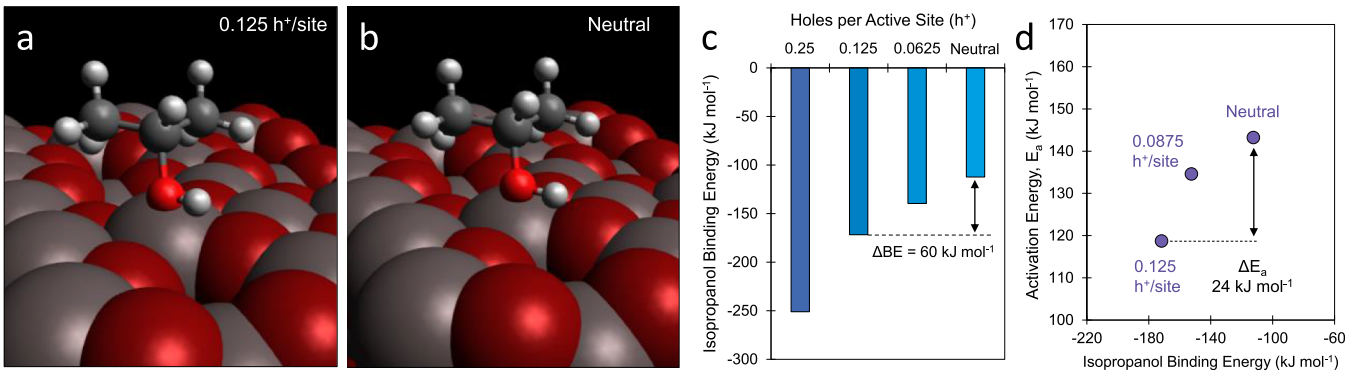

Figure 5. DFT calculations of IPA adsorption and dehydration on the Al_V^{3+} site of γ-alumina (100) as a function of charge. (a) 0.125 holes (h^+) per site with the $Al_V^{+3}-O^{IPA}$ bond distance of 1.963 Å, (b) neutral with the $Al_V^{+3}-O^{IPA}$ bond distance of 2.016 Å, (c) IPA binding energy versus hole density, and (d) associated activation energy to form propene and water from IPA. Color scheme: O—red, C—black, Al—grey, and H—white.

surface temperature did not vary more than one degree over 10 min for all considered applied potentials ($0 \leq V_{CAT} \leq +3$ V), thereby ruling out potential thermal artifacts.

Alternatively, the enhanced rate of IPA unimolecular dehydration under positive bias can be rationalized based on increased electron−hole density in the thin alumina−graphene layer, as indicated by capacitance measurements (Figure 2) and spectroscopy of the alumina film (Figure 3). Reduced electron density at the Lewis acid catalytic site of the aluminum oxide surface (Al_V^{3+}) increases site acidity, binding IPA stronger and reducing the catalytic activation barrier for its unimolecular dehydration to propene and water. The extent of positive charge condensation in the graphene-alumina active layer depends on the extent of applied potential bias as well as the design of the catalytic condenser stack. As summarized in Figure 2g, the number of electrons depleted in the aluminum oxide film at V_{CAT} of +3 V was measured to be 5.3×10^{12} e^- cm^{-2}; this is within an order of magnitude of pentacoordinate aluminum active site density available for acid catalysis reported on γ-Al_2O_3 ($10^{13}-10^{14}$ sites cm^{-2}).[13,38−40] It is therefore possible to deplete 0.05−0.50 electrons per active site at a potential bias V_{CAT} of +3 V. It should be noted that the amorphous 4 nm film atop the condenser may have an active site density distinct from γ-Al_2O_3, but it is unlikely to vary by more than an order of magnitude. The effect of this charge depletion at the active site can be further evaluated by computation, as described next.

IPA Binding and Dehydration Computed Energy

To simulate direct electron transfer to the alumina layer, we carried out periodic density functional theory (DFT) calculations whereby 0.25, 0.50, and 1.0 electrons were removed from a thin (6 Å) model Al_2O_3 slab. More specifically, we examined the dehydrated γ-Al_2O_3 (100) surface as a model alumina surface, as it is the lowest energy surface at the reaction conditions used in the experiments carried out herein with temperatures greater than 200 °C and partial pressures of water (P_{H2O}) > 10^{-3} bar.[13,41]

The removal of electrons from the thin Al_2O_3 slab increases the positive charge on the active Al_V^{3+} sites and increases the Lewis acidity. IPA then binds to the surface stronger. The adsorption energy decreases from −1.16 eV (112 kJ mol^{-1}, at zero charge) to −1.78 eV (−172 kJ $mole^{-1}$) as positive charge increases from 0 to 0.125 h^+ $site^{-1}$, as shown in Figure 5a−c. The IPA binding energy further strengthens as additional electron density is removed (Figure 5c). Naturally, the increased charge also results in shorter IPA $O^{IPA}-Al_V^{3+}$ bond distances; the $O^{IPA}-Al_V^{3+}$ bond decreases from 2.016 Å under neutral conditions to 1.963 Å for 0.125 h^+/site, as shown in Figure 5a,b.

Alcohol dehydration over alumina has been proposed to proceed over the $Al_{Va}^{3+}-O_{3b}^{2-}$ site pairs in a concerted E2 mechanism in which the C−OH and C−H bonds are simultaneously activated by the $Al_V^{3+}-O^{2-}$ acid−base site pairs to directly eliminate propene, which then desorbs.[13,38] $Al-(OH)^{\delta-}$ and $AlO-(H)^{\delta+}$ subsequently react to form and eliminate water. The calculated reactant, transition, and product states on the dehydrated γ-Al_2O_3 (100) surface are shown in Figure S29. The energetic pathways to form propene and water from IPA are summarized in Figure 5d, depicting the activation energy as a function of the IPA binding energy. The neutral alumina site dehydrates IPA with E_a of 143 kJ mol^{-1}, while the depleted alumina site (0.125 h^+/site), which has a higher Lewis acidity, has a lower barrier E_a of 119 kJ mol^{-1}. The barriers decrease monotonically with the positive charge (i.e., acidity) of the Al_V^{3+}sites and show the same trends as those found experimentally and shown in Figure 3c. The calculated barriers also decrease monotonically with the heat of IPA adsorption.

Catalytic Condenser Performance

The combined device characterization, spectroscopy, reaction experiments, and computation suggest that the active site of alumina has tunable acidity with the applied voltage, V_{CAT}. As suggested in Scheme 1, positive V_{CAT} depletes electrons in the catalytic alumina layer, most likely from the occupied in-gap states. The resulting electron-deficient aluminum site then binds IPA stronger and dehydrates it to propene with a lower activation barrier as larger V_{CAT} is applied. Calculated activation energies (Figure 5d) indicated that the IPA-to-propene activation barrier should reduce about 24 kJ mol^{-1} when 12.5% of an electron is depleted from an Al_V^{3+} active site. Comparison with experimental activation energies (Figure 3c) exhibiting ΔE_a of 16 kJ mol^{-1} for differences in applied biases of 0 and +3 V indicates that about 5−10% of an electron has been depleted per active site at an applied V_{CAT} of +3 V; this is consistent with the ratio of electron depletion (~5×10^{12} h^+ cm^{-2}, Figure 2) and alumina active site density (~5×10^{13} sites cm^{-2}).

Enhancing electron depletion at the active site for more acidic solid materials beyond the current catalytic condenser requires application of higher voltages, higher quality insulating

https://doi.org/10.1021/jacsau.2c00114
JACS Au 2022, 2, 1123−1133

(e.g., HfO_2) films, or alternative device design. The considered alumina/graphene catalytic condenser (70 nm HfO_2) stabilizes charge in a 4 nm alumina film. Thicker alumina films reduce the capability for electronically altering the surface acid site strength, as shown by experiments with a ∼50 nm alumina film on the alumina/graphene/HfO_2/p-Si catalytic condenser (Figure S20); alternatively, thinner alumina films can potentially stabilize more charge per active site. Additionally, application of a higher voltage V_{CAT} to the considered catalytic condenser (4 nm alumina film, graphene, 70 nm HfO_2) is problematic because leakage current through the device becomes substantial; this concept can be extended to higher voltages by further improving the quality of the HfO_2 film by reduction of pinholes. As a third design option, the condenser design can utilize different insulating materials such as higher-k dielectric materials (e.g., ferroelectrics) in thinner (<70 nm) insulating layers, both of which yield higher device capacitance and charge accumulation at the active site.

The electronically tunable nature of the alumina site in the catalytic condenser offers new capability for enhancing catalysis. While catalytic materials are conventionally tuned by precise synthesis of catalyst active sites, the limitation of material composition and stable structures only allows discrete options in active site design. In contrast, the bias potentials (V_{CAT}) to the active layer of a catalytic condenser can span a continuum of voltage bias values. Precise selection of the active site electronic state can potentially allow for optimization of selectivity to products or maximization of the catalytic rate.

Finally, the catalytic condenser design also allows for the capability to program catalysts that operate under continuous forced dynamic conditions.[1,42] Oscillation of the catalyst state yielding variation in the binding energy of the reactants and products has been predicted to increase the catalytic rate orders of magnitude at resonance conditions,[43] control the extent of reaction,[44] and allow for significant selectivity control to products.[45] Resonance conditions of the maximum catalytic rate are predicted to occur at varying frequencies depending on the extent of reactant binding energy variation (ΔBE), the composition and structure of the active site, and the nature of the chemistry of interest; but simulations have predicted catalytic resonance to occur for frequencies of ∼100 Hz up to 1 MHz.[42−47] For the considered catalytic condenser device, this requires depleting and replacing the electrons in the active sites at a comparable frequency. The time constant associated with electrons moving across the bare graphene surface (length of 1 cm) on HfO_2 was calculated to be 625 μs using the electron mobility (1600 $cm^2\ V^{-1}\ s^{-1}$), corresponding to a device operational frequency of 1600 Hz. Upon adding the alumina layer to the graphene device, electron mobility in the full device still permitted operation at ∼1000 Hz (see Supporting Information for the full calculations). The capability to program a repeating electronic perturbation of the catalyst (e.g., sinusoidal waveform of voltage bias) surface at high frequency (>1000 Hz) and amplitude (ΔBE > 0.4 eV) opens a new possibility for catalysts that change at the time scale of the catalytic turnover frequency.

CONCLUSIONS

A 1.0 cm^2 ML catalytic condenser device was synthesized by sequential deposition of 70 nm of amorphous HfO_2 on a conductive p-type Si wafer, followed by transfer of a graphene layer, on top of which was grown a 4 nm amorphous layer of the alumina catalyst. The HfO_2 layer remained amorphous below 400 °C with a dielectric constant of 26, providing a capacitance of ∼300 nF cm^{-2} and capability for stabilizing charge up to ∼5 × 10^{12} h^+/cm^2. Comparison of capacitance between two devices, one with graphene only and the other with alumina on graphene, indicated that the majority of the induced positive charge in the alumina/graphene device was actually in the aluminum oxide film. The alumina/graphene catalytic condenser with the HfO_2 insulator was observed to be conductive by scanning-tunneling microscopy with gap states located ∼0.3 eV below the Fermi level as determined by ultraviolet photoelectron spectroscopy. Dehydration of IPA on the alumina/graphene catalytic condenser top surface exhibited a variable peak temperature of propene formation in TPSR experiments. Propene peak temperatures, T_{peak}, shifted 50 °C with different potential biases (V_{CAT} of 0, +1, +2, +3 V), corresponding to a difference in activation energy of ΔE_a = 16 kJ mol^{-1} (0.17 eV). Enhanced Lewis acidity with positive V_{CAT} bias was consistent with increased IPA binding energy and reactivity to propene due to lower activation barriers as electrons were depleted at the surface active site, as calculated via DFT. The performance of the alumina/graphene catalytic condenser under bias indicates substantial potential for improving catalytic activity and tuning thermocatalytic selectivity, while oscillation of the alumina/graphene catalytic condenser via applied potential with large variation in surface acidity at frequencies as high as 1000 Hz achieves the conditions required for catalytic resonance.

METHODS

The alumina−graphene catalytic condenser was synthesized and then evaluated by electron microscopy, spectroscopy, experimental catalytic reaction, AFM, and computation. Full research methods are described in the Supporting Information.

Catalytic Condenser Fabrication

Devices were fabricated on a p-type Si substrate (WaferPro) using sequential deposition of HfO_2, graphene, an Au/Ti contact, and a thin amorphous alumina active layer. HfO_2 and alumina layers were grown within a flow-type ALD reactor (Kurt J Lesker ALD-150 LE). The 70-nm HfO_2 dielectric layer was grown via 500 HfO_2 ALD cycles at 100 °C. Each HfO_2 ALD cycle was composed of alternating exposures to Tetrakis(dimethylamido) hafnium (TDMAH, t = 13 ms) and H_2O (t = 200 ms) with purges in between each step. Graphene, obtained commercially on a Cu foil (Graphene Supermarket), was transferred on top of the HfO_2 layer using an existing PMMA-based method[21,22] and retained electrical conductivity (Figure S10). A small area (0.01 cm^2) contact (Au/Ti, 45 nm/5 nm) was then grown on the graphene by e-beam evaporation through a shadow mask. Finally, the catalytic alumina layer of ∼4 nm, based on the Al_2O_3 growth rate, was deposited via 50 Al_2O_3 ALD cycles at 100 °C using the same flow-type ALD reactor as mentioned above. Each Al_2O_3 ALD cycle was composed of alternating exposures to trimethylaluminum (TMA, t = 12 ms) and H_2O (t = 10,000 ms) with purges in between each step. Devices retained their structure after experimental reaction trials (Figures S23 and S24).

STEM, TEM, and SEM Analyses

Focused Ion Beam (FEI Helios NanoLab G4 dual-beam) was employed to prepare an electron-transparent cross-sectional lamella for the TEM and STEM study. An am-C layer (∼50 nm) was deposited on the device using the sputter coater as a protection layer. The additional protection layer consisted of am-C (2 μm) and Pt (2 μm) was deposited on the region of interest. FIB was operated at 30 kV with 5 kV electron beam. Conventional TEM, HAADF-STEM images, and STEM−EDX elemental maps were obtained using Thermo Fisher Talos F200X G2 S-TEM equipped with a Super-X energy-dispersive X-ray spectrometer. TEM and HAADF-STEM

https://doi.org/10.1021/jacsau.2c00114
JACS Au 2022, 2, 1123−1133

images were acquired at 200 kV. Camera length was set to be 125 mm with the probe convergence angle of 10.5 mrad for HAADF-STEM imaging. For EDX-mapping, beam current ranged from 300 pA to 400 pA. SEM images and SEM−EDX maps were acquired using JEOL 6500 FEG-SEM. SEM images and SEM−EDX elemental maps were obtained under 5 kV. The EDX maps were quantified using the Aztec EDX analytical system (Oxford Instruments). For more details, refer to the Supporting Information.

Spectroscopy

Raman spectra were obtained from a Witec Alpha 300R confocal Raman microscope equipped with a UHTS300 spectrometer and a DV401 CCD detector. XRD patterns were recorded on a Bruker D8 Discover 2D diffractometer equipped with a Co Kα source (λ = 0.179 nm). Full details are available in the Supporting Information. XPS measurements were performed on a PHI Versa Probe III XPS system (ULVAC-PHI) using a monochromated Al Kα X-ray source (1486.6 eV). The base pressure was 4.0×10^{-8} Pa. During data collection, the pressure was ca. 2.0×10^{-6} Pa. All samples were mounted on the holder using a Cu pin. The measurements were conducted using an X-ray spot size of 0.1×0.1 mm^2 with a power of 25 W under 15 kV. The survey spectra were measured using 280 eV pass energy and 1.0 eV/step. The data were processed with Multipak software. UPS measurements were performed on the same XPS system using ultraviolet radiation from an ionized He source. The base pressure was 8.0×10^{-7} Pa during measurement. The measurement spot size was approximately 6×6 mm^2. Survey spectra were measured using 1.3 eV pass energy and 0.025 eV per step.

Temperature-Programmed Surface Reaction

TPSR was carried out in a customized ultrahigh vacuum chamber reactor with IPA dehydration to propene as a reaction probe. The propene signal was monitored during the temperature ramp of the device, while voltage was applied. Full description of the equipment setup, device handling, temperature calibration, and the full TPSR process can be found in the Supporting Information.

Atomic Force Microscopy

AFM measurements were performed using a Bruker Dimension Icon closed-loop atomic force microscope using the force-modulation technique with a force feedback setpoint of 581 pN. Probes were standard Si cantilevers calibrated before measurement with a spring constant of 0.674 N m^{-1}.

Scanning Tunneling Microscopy

STM measurements were made using an Omicron low-temperature scanning tunneling microscope at room temperature under a vacuum of 8.0×10^{-10} mBar using a Pt/Ir probe. Samples were grounded through the alumina/graphene film. Differential spectra were collected from a Stanford Research Systems lock-in amplifier with a modulation signal of V_{mod} = 10 mV and f_{mod} = 10 kHz. Data were processed using the WSxM software.

Computation

First principles periodic DFT calculations were carried out to determine the binding energies and the activation barriers using the plane wave implementation of DFT in the Vienna ab initio simulation package (VASP).[48−50] The generalized gradient approximation form of the Perdew, Burke, and Ernzerhof functional was used to determine the energies, and dispersion corrections were included via the D3 corrections developed by Grimme.[51,52] An energy cutoff of 400 eV was used in the construction of plane waves, and projector augmented wave potentials were used to model interactions between core and valence electrons.[53,54] A periodic slab of 2×2 times the primitive unit cell and consisting of seven layers of γ-Al_2O_3 (100) was used for all calculations, with the bottom-most layer held fixed. All electronic energies were converged to within a tolerance of 10^{-6} eV using a $2 \times 1 \times 1$ gamma-centered k-point grid. The geometries of the structures were optimized until the maximum force on each atom was calculated to be less than 0.05 eV Å^{-1}. Additional details are provided in the Supporting Information.

ASSOCIATED CONTENT

Supporting Information

The Supporting Information is available free of charge at https://pubs.acs.org/doi/10.1021/jacsau.2c00114.

Catalytic condenser fabrication methods, TEM and SEM characterization, reactor setup, reaction process, and control experiments, electronic characterization, XRD, Redhead analysis of TPSRs, and additional references 55 and 56 (PDF)

AUTHOR INFORMATION

Corresponding Author

Paul J. Dauenhauer − *Department of Chemical Engineering & Materials Science, University of Minnesota, Minneapolis, Minnesota 55455, United States;* orcid.org/0000-0001-5810-1953; Email: hauer@umn.edu

Authors

Tzia Ming Onn − *Department of Chemical Engineering & Materials Science, University of Minnesota, Minneapolis, Minnesota 55455, United States*

Sallye R. Gathmann − *Department of Chemical Engineering & Materials Science, University of Minnesota, Minneapolis, Minnesota 55455, United States*

Yuxin Wang − *Department of Chemical Engineering & Materials Science, University of Minnesota, Minneapolis, Minnesota 55455, United States*

Roshan Patel − *Department of Chemical Engineering & Materials Science, University of Minnesota, Minneapolis, Minnesota 55455, United States;* orcid.org/0000-0003-4826-1536

Silu Guo − *Department of Chemical Engineering & Materials Science, University of Minnesota, Minneapolis, Minnesota 55455, United States*

Han Chen − *Department of Chemical Engineering, University of Massachusetts Amherst, Amherst, Massachusetts 01003, United States;* orcid.org/0000-0002-8262-4196

Jimmy K. Soeherman − *Department of Chemical Engineering & Materials Science, University of Minnesota, Minneapolis, Minnesota 55455, United States*

Phillip Christopher − *Department of Chemical Engineering, University of California, Santa Barbara, Santa Barbara, California 93106, United States;* orcid.org/0000-0002-4898-5510

Geoffrey Rojas − *Characterization Facility, University of Minnesota, Minneapolis, Minnesota 55455, United States*

K. Andre Mkhoyan − *Department of Chemical Engineering & Materials Science, University of Minnesota, Minneapolis, Minnesota 55455, United States;* orcid.org/0000-0003-3568-5452

Matthew Neurock − *Department of Chemical Engineering & Materials Science, University of Minnesota, Minneapolis, Minnesota 55455, United States;* orcid.org/0000-0003-1458-7837

Omar A. Abdelrahman − *Department of Chemical Engineering, University of Massachusetts Amherst, Amherst, Massachusetts 01003, United States;* orcid.org/0000-0001-6023-857X

C. Daniel Frisbie − *Department of Chemical Engineering & Materials Science, University of Minnesota, Minneapolis,*

Minnesota 55455, United States; orcid.org/0000-0002-4735-2228

Complete contact information is available at: https://pubs.acs.org/10.1021/jacsau.2c00114

Notes

The authors declare no competing financial interest.

■ ACKNOWLEDGMENTS

We acknowledge financial support from the U.S. Department of Energy, Basic Energy Sciences Catalysis program (DE-SC0021163) and the National Science Foundation CBET-Catalysis program (award #1937641). S.R.G. was supported by the National Science Foundation Graduate Research Fellowship under Grant CON-75851, project 00074041. S.G. and K.A.M. were supported by University of Minnesota (UMN) MRSEC program DMR-2011401. The electron microscopy work was carried out in the Characterization Facility of University of Minnesota supported in part by the NSF through the UMN MRSEC. We thank Keith and Amy Steva for their generous support of this project through their donor advised fund. We thank Professor Aditya Bhan for helpful conversations.

■ REFERENCES

(1) Shetty, M.; Walton, A.; Gathmann, S. R.; Ardagh, M. A.; Gopeesingh, J.; Resasco, J.; Birol, T.; Zhang, Q.; Tsapatsis, M.; Vlachos, D. G.; Christopher, P.; Frisbie, C. D.; Abdelrahman, O. A.; Dauenhauer, P. J. The Catalytic Mechanics of Dynamic Surfaces: Stimulating Methods for Promoting Catalytic Resonance. *ACS Catal.* **2020**, *10*, 12666−12695.

(2) Alves, L. F. S.; Lefranc, P.; Jeannin, P.-O.; Sarrazin, B. Review on SiC-MOSFET Devices and Associated Gate Drivers. *Proc. IEEE Int. Conf. Ind. Technol.* **2018**, *2018*, 824−829.

(3) Kim, C.-H.; Frisbie, C. D. Field Effect Modulation of Outer-Sphere Electrochemistry at Back-Gated, Ultrathin ZnO Electrodes. *J. Am. Chem. Soc.* **2016**, *138*, 7220−7223.

(4) Wang, Y.; Kim, C.-H.; Yoo, Y.; Johns, J. E.; Frisbie, C. D. Field Effect Modulation of Heterogeneous Charge Transfer Kinetics at Back-Gated Two-Dimensional MoS2 Electrodes. *Nano Lett.* **2017**, *17*, 7586−7592.

(5) Wang, Y.; Udyavara, S.; Neurock, M.; Frisbie, C. D. Field Effect Modulation of Electrocatalytic Hydrogen Evolution at Back-Gated Two-Dimensional MoS2 Electrodes. *Nano Lett.* **2019**, *19*, 6118−6123.

(6) Wu, Y.; Ringe, S.; Wu, C.-L.; Chen, W.; Yang, A.; Chen, H.; Tang, M.; Zhou, G.; Hwang, H. Y.; Chan, K.; Cui, Y. A Two-Dimensional MoS2 Catalysis Transistor by Solid-State Ion Gating Manipulation and Adjustment (SIGMA). *Nano Lett.* **2019**, *19*, 7293−7300.

(7) Shi, B. C.; Davis, B. H. Alcohol Dehydration: Mechanism of Ether Formation Using an Alumina Catalyst. *J. Catal.* **1995**, *157*, 359−367.

(8) Narayanan, C.; Srinivasan, S.; Datye, A. K.; Gorte, R.; Biaglow, A. The Effect of Alumina Structure on Surface Sites for Alcohol Dehydration. *J. Catal.* **1992**, *138*, 659−674.

(9) de Boer, J.; Fahim, R. B.; Linsen, B. G.; Visseren, W. J.; de Vleesschauwer, W. F. N. M. Kinetics of the Dehydration of Alcohol on Alumina. *J. Catal.* **1967**, *7*, 163−172.

(10) Pines, H.; Haag, W. O. Alumina: Catalyst and Support. I. Alumina, its Intrinsic Acidity and Catalytic Activity1. *J. Am. Chem. Soc.* **1960**, *82*, 2471−2483.

(11) Trueba, M.; Trasatti, S. P. γ-Alumina as a Support for Catalysts: A Review of Fundamental Aspects. *Eur. J. Inorg. Chem.* **2005**, *2005*, 3393−3403.

(12) Arai, H.; Take, J. I.; Saito, Y.; Yoneda, Y. Ethanol dehydration on alumina catalysts I. The thermal desorption of surface compounds. *J. Catal.* **1967**, *9*, 146−153.

(13) Roy, S.; Mpourmpakis, G.; Hong, D.-Y.; Vlachos, D. G.; Bhan, A.; Gorte, R. J. Mechanistic Study of Alcohol Dehydration on γ-Al2O3. *ACS Catal.* **2012**, *2*, 1846−1853.

(14) Balzarotti, A.; Bianconi, A. Electronic Structure of Aluminium Oxide as Determined by X-Ray Photoemission. *Phys. Status Solidi* **1976**, *76*, 689−694.

(15) Ealet, B.; Elyakhloufi, M. H.; Gillet, E.; Ricci, M. Electronic and Crystallographic Structure of γ-Alumina Thin Films. *Thin Solid Films* **1994**, *250*, 92−100.

(16) Jimenéz-Gonzaléz, A.; Schmeisser, D. Preparation and Spectroscopic Characterization of γ-Al2O3 Thin Films. *Surf. Sci.* **1991**, *250*, 59−70.

(17) Jenness, G. R.; Christiansen, M. A.; Caratzoulas, S.; Vlachos, D. G.; Gorte, R. J. Site-Dependent Lewis Acidity of γ-Al2O3 and Its Impact on Ethanol Dehydration and Etherification. *J. Phys. Chem. C* **2014**, *118*, 12899−12907.

(18) Hu, J. Z.; Xu, S.; Kwak, J. H.; Hu, M. Y.; Wan, C.; Zhao, Z.; Szanyi, J.; Bao, X.; Han, X.; Wang, Y.; Peden, C. H. F. High Field 27Al MAS NMR and TPD Studies of Active Sites in Ethanol Dehydration Using Thermally Treated Transitional Aluminas as Catalysts. *J. Catal.* **2016**, *336*, 85−93.

(19) Blaschke, D.; Munnik, F.; Grenzer, J.; Rebohle, L.; Schmidt, H.; Zahn, P.; Gemming, S. A correlation study of layer growth rate, thickness uniformity, stoichiometry, and hydrogen impurity level in HfO2 thin films grown by ALD between 100°C and 350°C. *Appl. Surf. Sci.* **2020**, *506*, 144188.

(20) Gierałtowska, S.; Sztenkiel, D.; Guziewicz, E.; Godlewski, M.; Łuka, G.; Witkowski, B. S.; Wachnicki, Ł.; Łusakowska, E.; Dietl, T.; Sawicki, M. Properties and Characterization of ALD Grown Dielectric Oxides for MIS Structures. *Acta Phys. Pol., A* **2011**, *119*, 692−695.

(21) Suk, J. W.; Kitt, A.; Magnuson, C. W.; Hao, Y.; Ahmed, S.; An, J.; Swan, A. K.; Goldberg, B. B.; Ruoff, R. S. Transfer of CVD-Grown Monolayer Graphene onto Arbitrary Substrates. *ACS Nano* **2011**, *5*, 6916−6924.

(22) Reina, A.; Son, H.; Jiao, L.; Fan, B.; Dresselhaus, M. S.; Liu, Z.; Kong, J. Transferring and Identification of Single- and Few-Layer Graphene on Arbitrary Substrates. *J. Phys. Chem. C* **2008**, *112*, 17741−17744.

(23) Böscke, T. S.; Govindarajan, S.; Kirsch, P. D.; Hung, P. Y.; Krug, C.; Lee, B. H.; Heitmann, J.; Schröder, U.; Pant, G.; Gnade, B. E.; Krautschneider, W. H. Stabilization of higher-κ tetragonal HfO2 by SiO2 admixture enabling thermally stable metal-insulator-metal capacitors. *Appl. Phys. Lett.* **2007**, *91*, 072902.

(24) Böscke, T. S.; Govindarajan, S.; Fachmann, C.; Heitmann, J.; Avellan, A.; Schroder, U.; Kudelka, S.; Kirsch, P. D.; Krug, C.; Hung, P. Y.; Song, S. C.; Ju, B. S.; Price, J.; Pant, G.; Gnade, B. E.; Krautschneider, W.; Lee, B.-H.; Jammy, R. Tetragonal Phase Stabilization by Doping as an Enabler of Thermally Stable HfO2 Based MIM and MIS Capacitors for Sub 50nm Deep Trench DRAM. *Tech. Dig. - Int. Electron Devices Meet.* **2006**, 1−4.

(25) Vervuurt, R. H. J.; Karasulu, B.; Verheijen, M. A.; Kessels, W. M. M.; Bol, A. A. Uniform Atomic Layer Deposition of Al2O3 on Graphene by Reversible Hydrogen Plasma Functionalization. *Chem. Mater.* **2017**, *29*, 2090−2100.

(26) Schilirò, E.; Lo Nigro, R.; Roccaforte, F.; Giannazzo, F. Substrate-Driven Atomic Layer Deposition of High-κ Dielectrics on 2D Materials. *Appl. Sci.* **2021**, *11*, 11052.

(27) Zhang, Y.; Qiu, Z.; Cheng, X.; Xie, H.; Wang, H.; Xie, X.; Yu, Y.; Liu, R. Direct Growth of High-Quality Al2O3 Dielectric on Graphene Layers by Low-Temperature H2O-Based ALD. *J. Phys. D: Appl. Phys.* **2014**, *47*, 055106.

(28) Wang, M.; Huang, M.; Luo, D.; Li, Y.; Choe, M.; Seong, W. K.; Kim, M.; Jin, S.; Wang, M.; Chatterjee, S.; Kwon, Y.; Lee, Z.; Ruoff, R. S. Single-Crystal, Large-Area, Fold-Free Monolayer Graphene. *Nature* **2021**, *596*, 519−524.

(29) Johnson, R. W.; Hultqvist, A.; Bent, S. F. A Brief Review of Atomic Layer Deposition: From Fundamentals to Applications. *Mater. Today* **2014**, *17*, 236−246.
(30) Jeong, S.-J.; Gu, Y.; Heo, J.; Yang, J.; Lee, C.-S.; Lee, M.-H.; Lee, Y.; Kim, H.; Park, S.; Hwang, S. Thickness Scaling of Atomic-Layer-Deposited HfO2 Films and Their Application to Wafer-Scale Graphene Tunnelling Transistors. *Sci. Rep.* **2016**, *6*, 20907.
(31) Jung, H.-S.; Jang, J. H.; Cho, D.-Y.; Jeon, S.-H.; Kim, H. K.; Lee, S. Y.; Hwang, C. S. The Effects of Postdeposition Annealing on the Crystallization and Electrical Characteristics of HfO2 and ZrO2 Gate Dielectrics. *Electrochem. Solid-State Lett.* **2011**, *14*, G17.
(32) Xie, Y.; Ma, Z.; Su, Y.; Liu, Y.; Liu, L.; Zhao, H.; Zhou, J.; Zhang, Z.; Li, J.; Xie, E. The Influence of Mixed Phases on Optical Properties of HfO2 Thin Films Prepared by Thermal Oxidation. *J. Mater. Res.* **2011**, *26*, 50−54.
(33) He, G.; Liu, M.; Zhu, L. Q.; Chang, M.; Fang, Q.; Zhang, L. D. Effect of postdeposition annealing on the thermal stability and structural characteristics of sputtered HfO2 films on Si (100). *Surf. Sci.* **2005**, *576*, 67−75.
(34) Zhang, X.-Y.; Hsu, C.-H.; Lien, S.-Y.; Wu, W.-Y.; Ou, S.-L.; Chen, S.-Y.; Huang, W.; Zhu, W.-Z.; Xiong, F.-B.; Zhang, S. Temperature-Dependent HfO2/Si Interface Structural Evolution and Its Mechanism. *Nanoscale Res. Lett.* **2019**, *14*, 83.
(35) Vargas, M.; Murphy, N. R.; Ramana, C. V. Structure and Optical Properties of Nanocrystalline Hafnium Oxide Thin Films. *Opt. Mater.* **2014**, *37*, 621−628.
(36) Moon, J.-Y.; Kim, M.; Kim, S.-I.; Xu, S.; Choi, J.-H.; Whang, D.; Watanabe, K.; Taniguchi, T.; Park, D. S.; Seo, J.; Cho, S. H.; Son, S.-K.; Lee, J.-H. Layer-Engineered Large-Area Exfoliation of Graphene. *Sci. Adv.* **2020**, *6*, abc6601.
(37) Redhead, P. A. Thermal Desorption of Gases. *Vacuum* **1962**, *12*, 203−211.
(38) Kostestkyy, P.; Yu, J.; Gorte, R. J.; Mpourmpakis, G. Structure-Activity Relationships on Metal-Oxides: Alcohol Dehydration. *Catal. Sci. Technol.* **2014**, *4*, 3861−3869.
(39) Guillaume, D.; Gautier, S.; Despujol, I.; Alario, F.; Beccat, P. Characterization of Acid Sites on γ-Alumina and Chlorinated γ-Alumina By31P NMR of Adsorbed Trimethylphosphine. *Catal. Lett.* **1997**, *43*, 213−218.
(40) Zhai, Y.; Pierre, D.; Si, R.; Deng, W.; Ferrin, P.; Nilekar, A. U.; Peng, G.; Herron, J. A.; Bell, D. C.; Saltsburg, H.; Mavrikakis, M.; Flytzani-Stephanopoulos, M. Alkali-Stabilized Pt-OH x Species Catalyze Low-Temperature Water-Gas Shift Reactions. *Science* **2010**, *329*, 1633−1636.
(41) Kwak, J. H.; Mei, D.; Peden, C. H. F.; Rousseau, R.; Szanyi, J. (100) facets of γ-Al2O3: The Active Surfaces for Alcohol Dehydration Reactions. *Catal. Lett.* **2011**, *141*, 649−655.
(42) Gathmann, S. R.; Ardagh, M. A.; Dauenhauer, P. J. Catalytic Resonance Theory: Negative Dynamic Surfaces for Programmable Catalysts. *Chem. Catal.* **2022**, *2*, 140−163.
(43) Ardagh, M. A.; Abdelrahman, O. A.; Dauenhauer, P. J. Principles of Dynamic Heterogeneous Catalysis: Surface Resonance and Turnover Frequency Response. *ACS Catal.* **2019**, *9*, 6929−6937.
(44) Ardagh, M. A.; Birol, T.; Zhang, Q.; Abdelrahman, O. A.; Dauenhauer, P. J. Catalytic Resonance Theory: SuperVolcanoes, Catalytic Molecular Pumps, and Oscillatory Steady State. *Catal. Sci. Technol.* **2019**, *9*, 5058−5076.
(45) Alexander Ardagh, M.; Shetty, M.; Kuznetsov, A.; Zhang, Q.; Christopher, P.; Vlachos, D. G.; Abdelrahman, O. A.; Dauenhauer, P. J. Catalytic Resonance Theory: Parallel Reaction Pathway Control. *Chem. Sci.* **2020**, *11*, 3501−3510.
(46) Gopeesingh, J.; Ardagh, M. A.; Shetty, M.; Burke, S. T.; Dauenhauer, P. J.; Abdelrahman, O. A. Resonance-Promoted Formic Acid Oxidation via Dynamic Electrocatalytic Modulation. *ACS Catal.* **2020**, *10*, 9932−9942.
(47) Wittreich, G. R.; Liu, S.; Dauenhauer, P. J.; Vlachos, D. G. Catalytic Resonance of Ammonia Synthesis by Simulated Dynamic Ruthenium Crystal Strain. *Sci. Adv.* **2022**, *8*, No. eabl6576.
(48) Kresse, G.; Hafner, J. Ab initio molecular dynamics for liquid metals. *Phys. Rev. B* **1993**, *47*, 558−561.
(49) Kresse, G.; Hafner, J. Ab initio molecular-dynamics simulation of the liquid-metal-amorphous-semiconductor transition in germanium. *Phys. Rev. B* **1994**, *49*, 14251−14269.
(50) Kresse, G.; Furthmüller, J. Efficient iterative schemes for ab initio total-energy calculations using a plane-wave basis set. *Phys. Rev. B: Condens. Matter Mater. Phys.* **1996**, *54*, 11169−11186.
(51) Perdew, J. P.; Burke, K.; Ernzerhof, M. Generalized Gradient Approximation Made Simple. *Phys. Rev. Lett.* **1996**, *77*, 3865−3868.
(52) Grimme, S.; Antony, J.; Ehrlich, S.; Krieg, H. A Consistent and Accurate Ab Initio Parametrization of Density Functional Dispersion Correction (DFT-D) for the 94 Elements H-Pu. *J. Chem. Phys.* **2010**, *132*, 154104.
(53) Kresse, G.; Joubert, D. From Ultrasoft Pseudopotentials to the Projector Augmented-Wave Method. *Phys. Rev. B: Condens. Matter Mater. Phys.* **1999**, *59*, 1758−1775.
(54) Blöchl, P. E. Projector Augmented-Wave Method. *Phys. Rev. B* **1994**, *50*, 17953−17979.
(55) Blanck, S.; Martí, C.; Loehlé, S.; Steinmann, S. N.; Michel, C. (Dis)Similarities of Adsorption of Diverse Functional Groups over Alumina and Hematite Depending on the Surface State. *J. Chem. Phys.* **2021**, *154*, 084701.
(56) Henkelman, G.; Jónsson, H. Improved Tangent Estimate in the Nudged Elastic Band Method for Finding Minimum Energy Paths and Saddle Points. *J. Chem. Phys.* **2000**, *113*, 9978−9985.

https://doi.org/10.1021/jacsau.2c00114
JACS Au 2022, 2, 1123−1133